

Antarctic Infrared Binocular Telescope: Early Data Release of observations in the 1.4 μm water-vapor-absorption band

PU LIN(林浦) ,¹ HAONAN YANG(杨浩楠) ,¹ BIN MA(马斌) ,^{1,2} JINJI LI(李晋基) ,¹ HAORAN ZHANG(张皓然) ,¹ MICHAEL C. B. ASHLEY ,³ ZHONGNAN DONG(董仲南) ,^{1,4} LU FENG(冯麓),⁴ WEI HUANG(黄伟) ,¹ YI HU(胡义) ,⁴ ZHAOHUI SHANG(商朝晖) ,⁴ YUN SHI(史韵) ,¹ SHIJIE SUN(孙士杰) ,⁴ XU YANG(杨栩) ,⁴ AND YONG ZHANG(张泳) ,^{1,2}

¹ School of Physics and Astronomy, Sun Yat-sen University, Zhuhai 519082, People's Republic of China

² CSST Science Center for the Guangdong-Hong Kong-Macau Greater Bay Area, Zhuhai 519082, People's Republic of China

³ School of Physics, University of New South Wales, Sydney, NSW 2052, Australia

⁴ National Astronomical Observatories, Chinese Academy of Sciences, Beijing 100101, China

Submitted to xxx

ABSTRACT

Ground-based observations around 1.4 μm are normally limited by strong absorption of telluric water-vapor. However, Dome A, Antarctica has exceptionally dry conditions that offer a unique opportunity for observations in this band. We designed a new filter covering 1.34–1.48 μm , namely W' , and installed it on the Antarctic Infrared Binocular Telescope (AIRBT) at Dome A in 2025. AIRBT comprises two identical 15 cm optical tube assemblies and two InGaAs cameras equipped with J and W' filters, respectively. With this Early Data Release (EDR), we aim to evaluate the performance of the W' band at Dome A to observe objects with water-vapor features. This EDR covers ~ 20 deg² in the Galactic plane using $\sim 20,000$ images in three nights. For 2 s exposures, the 5 σ limiting magnitude histogram peaks at $J \sim 11.5$ mag (Vega) and $W' \sim 9.9$ mag, respectively. The $J - W'$ vs $J - H$ color-color diagram distinguishes ultracool candidates with water-vapor-absorption features from reddened early type stars. Furthermore, later-type stars tend to exhibit stronger water-vapor absorption. Some sources show larger $\Delta W'$ than ΔJ across the three nights, which we attribute to variations of their water-vapor-absorption depth. We conclude that it will be efficient to search for ultracool stars and estimate their spectral subtypes using W' band imaging at Dome A, where the atmospheric transmission is high and stable.

Keywords: Catalogs (205) — Near infrared astronomy (1093) — Stellar atmospheres (1584) — Photometry (1234)

1. INTRODUCTION

Water plays a crucial role in the study of astronomy. Observations show that water is widely found in the universe (e.g., E. F. van Dishoeck et al. 2013). In cool giants, water-vapor-absorption features reflect the structure and molecular composition of their outer atmospheres. Spectroscopic studies of Mira variables have shown that water-vapor in their atmospheres influences atmospheric convection and pulsational behavior

(M. Wittkowski et al. 2016). Water is also present in molecular clouds that undergo star formation and plays an important role in their chemistry and evolution (E. A. Bergin & W. D. Langer 1997; E. A. Bergin & M. Tafalla 2007; E. F. van Dishoeck et al. 2014; E. F. van Dishoeck et al. 2021). In exoplanet atmospheres, water influences dynamics and solid accretion during planetary evolution (F. J. Ciesla & J. N. Cuzzi 2006; K. Ros & A. Johansen 2013); moreover, water's abundance and chemical form strongly affect a planet's habitability and are crucial to studies of the origin of life (S. Krijt et al. 2023).

Water exists as vapor in the atmosphere of ultracool stars, brown dwarfs, and exoplanets. Consequently, wa-

ter produces many wide and deep absorption features in infrared spectra. Spectroscopic observations show that cool giants and dwarfs exhibit absorption features near $1.4 \mu\text{m}$ caused by water-vapor, and that the lower the temperature (i.e. the later the spectral type), the deeper the absorption (J. T. Rayner et al. 2009). Therefore, these features can be used for batch classification, candidate search, and spectral type estimation. In exoplanet atmospheric studies, water-vapor-absorption is a crucial tool to find potential habitable planets. For example, a JWST transit spectroscopic observation of WASP-96b revealed water-vapor-absorption peaks in the infrared, confirming the presence of water-vapor in its atmosphere (J. Taylor et al. 2023; M. Radica et al. 2023). Through water-vapor-absorption near $1.4 \mu\text{m}$, HST transit observations detected water-vapor in the atmosphere of the hot Jupiter HD 189733b (J. Fraine et al. 2014) and the Neptune-sized exoplanet HAT-P-11b (P. McCullough et al. 2014).

Observing water-vapor features in astrophysical objects from the surface of the Earth is challenging due to the water-vapor content in the Earth's atmosphere and particularly by its variability. That is why most current observations in the promising $1.4 \mu\text{m}$ band rely mainly on space telescopes such as HST/WFC3 with F139M/F140W (L. Dressel et al. 2016) filters and JWST/NIRCam with F140M/F150W⁵. K. N. Allers & M. C. Liu (2020) have developed a W filter with a central wavelength of $1.45 \mu\text{m}$ and a bandpass width of 6% ($\sim 87 \text{ nm}$), which covers part of the water-vapor-absorption region, while avoiding the area with the strongest atmospheric absorption at Mauna Kea. With the W imaging, they efficiently distinguished late M and L dwarfs from reddened background stars in star-forming regions. They estimated spectral types with a precision of 1.4 subtypes on the basis of the absorption depth.

Dome A in Antarctica is an ideal site for ground-based observations (Z. Shang 2020; B. Ma et al. 2020; X. Yang et al. 2021; Y. Hu et al. 2018), and especially its extremely dry condition, an almost perfect site for $1.4 \mu\text{m}$ observation because of its extremely dry air. The median precipitable water vapor (PWV) is about 0.13–0.14 mm (H. Yang et al. 2010; G. Sims et al. 2012; C.-L. Kuo 2017; S.-C. Shi et al. 2016), yielding a high atmospheric transmission near $1.4 \mu\text{m}$ (G. Sims et al. 2012). To verify the performance of this new window at Dome A, we designed a new filter, W' , covering $1.34\text{--}1.48 \mu\text{m}$ (H. Zhang & B. Ma 2024). Compared with the original W filter at Mauna Kea (K. N. Allers & M. C. Liu 2020),

our W' filter is broader and more transparent at Dome A, which will improve observational efficiency. Figure 1 compares the atmosphere transmission at Dome A (H. Zhang & B. Ma 2024) and Mauna Kea⁶ together with the filter transmission curve of AIRBT and 2MASS (M. Cohen et al. 2003).

In 2025 we installed the W' filter in one of the telescopes in the Antarctic Infrared Binocular Telescope (AIRBT) (Z. Dong et al. 2025), replacing the original H' filter. Our observations with the W' filter aim to search for and study ultracool giants and dwarfs by detecting their water-vapor-absorption features, and to estimate their spectral types. In this paper, we present an Early Data Release (EDR) of AIRBT observations in 2025, and explore the scientific potential of the W' filter. The paper is organized as follows: Sect. 2 introduces AIRBT and the observation data in the EDR; Sect. 3 describes the data reduction and photometric calibration; Sect. 4 presents photometric results, data products, and direct analysis from catalogs, including using the color-color diagram and variability to search for candidates with water-vapor-absorption; Sect. 5 discusses the correlation between water-vapor-absorption and spectral type, and examines the atmospheric transmission stability at Dome A; Sect. 6 provides a summary and our future plans.

2. TELESCOPE AND OBSERVATIONS

2.1. Telescope overview

AIRBT (see upper left Fig. 2) comprises two 15 cm optical tube assemblies in a Ritchey-Chr é tien (RC) design with a lens corrector and a f/3 focal ratio. Each focal plane array consists of a commercial InGaAs camera with 640×512 pixel $15 \mu\text{m}$ pixels, giving a pixel scale of $6.84'' \text{ pixel}^{-1}$ and a field-of-view (FoV) of $1.22^\circ \times 0.97^\circ$.

After technical validation in China in October 2022 (Z. Dong et al. 2025), AIRBT was installed at Dome A, Antarctica in January 2023 by the 39th China National Antarctic Research Expedition (CHINARE 39). After maintenance in January 2024 by CHINARE 40, AIRBT carried out time domain surveys in J and H simultaneously. During maintenance in January 2025 by CHINARE 41, AIRBT's H filter was replaced with a W' filter and began observations in the J and W' bands. All power and data transfer were provided through the PLATEau Observatory for Dome A (PLATO-A, J. Lawrence et al. 2009; M. C. B. Ashley et al. 2010) platform.

⁵ <https://jwst-docs.stsci.edu/jwst-near-infrared-camera/nircam-instrumentation/nircam-filters>

⁶ <https://www.gemini.edu/observing/telescopes-and-sites/sites%23MKWV#Transmission>

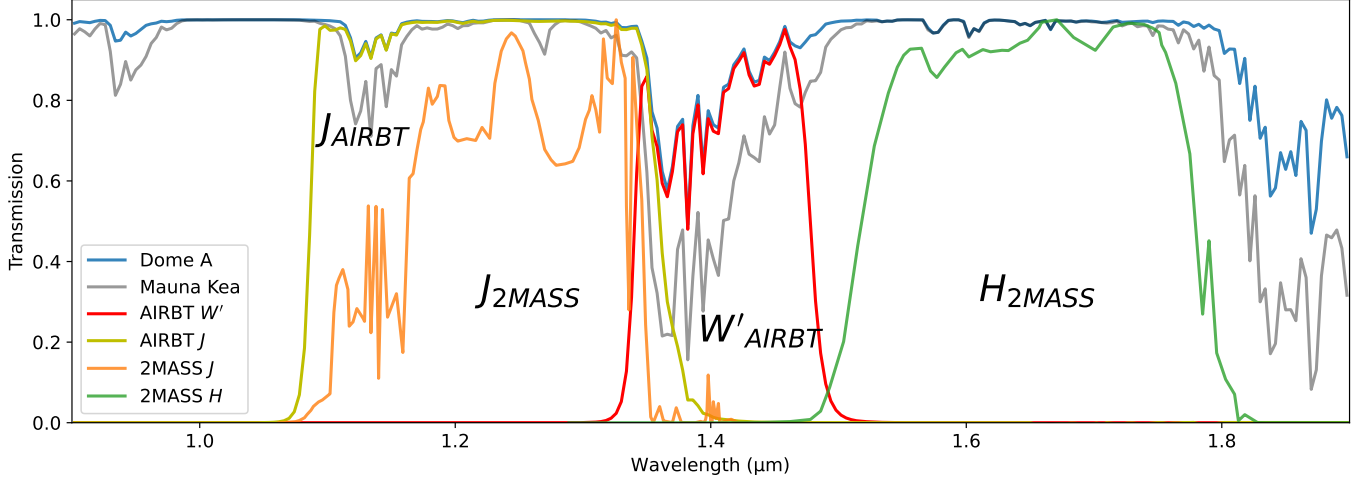


Figure 1. Theoretical atmosphere transmission at Dome A (blue, median PWV = 0.141 mm, airmass = 1.0) and Mauna Kea (gray, median PWV = 1.6 mm, airmass = 1.0) at a 4 nm resolution, and filter transmission curves of AIRBT J , W' filters and 2MASS J , H filters. All filter transmission curves include the effect of atmosphere transmission.

As the transmission curves show in Fig. 1, the W' filter is specially designed to cover the entire water-vapor-absorption region near $1.4\ \mu\text{m}$. Additionally, compared with 2MASS, our J filter is broader to increase SNR and its blue-ward side has larger efficiency because of atmosphere transmission at Dome A.

2.2. Observations

AIRBT's observations in the J and W' bands began in January 2025 as tests of system stability and performance. During February, with the Sun continuously above the horizon at Dome A, we were restricted to monitoring several bright stars. From 16 March, with the night emerging, the telescope conducted continuous observations until 23 April, when a communication issue suspended operations. During the night-time observations, the telescope was operated in drift scan mode due to mechanical issues with the mount, so observations were restricted to the sky drifting naturally across the FoV.

We selected the Galactic plane as the primary area of interest due to high star density and strong interstellar extinction, which can highlight our advantages. Strong interstellar extinction reddens stars to varying degrees, thereby reducing the reliability of spectral type identification using broadband colors. In contrast, water-vapor-absorption features near $1.4\ \mu\text{m}$ are essentially unaffected by extinction, thus offering a more reliable method for estimating spectral types. To observe the Galactic plane we fixed the pointing at declination of $\delta = -61.3^\circ$, while minimizing air mass by pointing almost due north; the image center was at $ALT = 358.265^\circ$ and $AZ = 71.375^\circ$,

The images were automatically captured, with exposure times adjusted according to the background from daytime to nighttime. The maximum exposure time was set to 2 s to balance PSF elongation and observation efficiency. During the nighttime, a group of 200 exposures was captured at a time, with about 40 s overhead between groups. During observations, we power on the Indium-Tin-Oxide (ITO) films coated on the windows to warm the windows and consequently prevent frost accumulation. The ITO performance was remarkably effective (see Fig. 13) while having a negligible effect on image quality (see Fig. 7).

The J and W' detectors had different X-Y orientations because of mounting restrictions, thus the FoVs of the J and W' bands did not fully overlap, as the upper right panel of Fig. 2 shows. The overlapping area of J and W' bands covers $\delta = -61.7^\circ \sim -61.0^\circ$, and a star drifting through it stays within it for about eight minutes. The coverage of RA was dependent on the length of the night, with $\alpha = 145^\circ \sim 205^\circ$ for the first night (16 March 2025), and $\alpha = 75^\circ \sim 350^\circ$ for the last night (22 April 2025), as the gray markers show in the lower panel of Fig. 2.

All raw data were stored at Dome A and partially downloaded via internet from the PLATO-A platform. The full data are scheduled to be retrieved by the next traverse. In this paper, we selected three nights (16 March, 3 April, and 20 April 2025) for this Early Data Release (EDR); these nights correspond to the beginning, middle, and end of the observing period. Our aims with the EDR are to evaluate the telescope's performance and to explore the scientific potential of the W' filter. The overlapping area of those three nights covers $\alpha = 145^\circ \sim 205^\circ$ and lies entirely within the Galactic

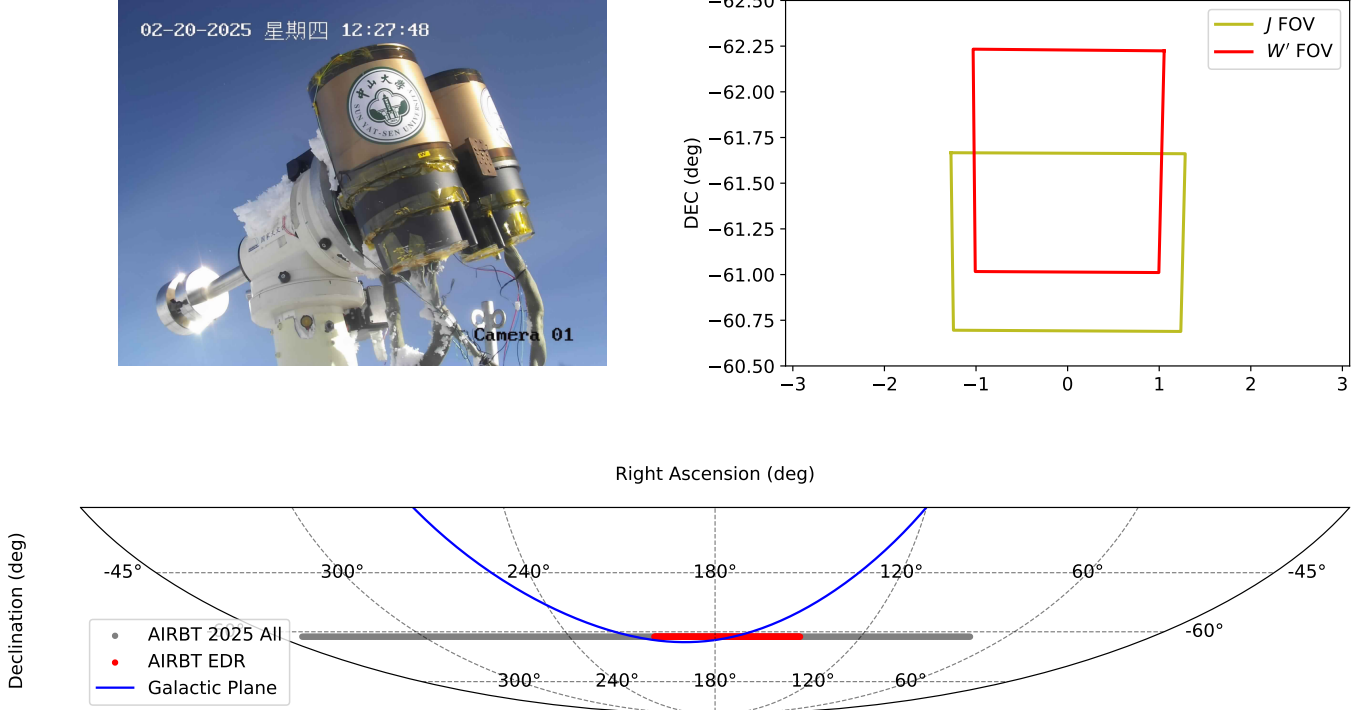


Figure 2. Upper Left: The Antarctica Infrared Binocular Telescope (AIRBT) at Dome A, Antarctica. Upper Right: The FoVs of the J (shown in yellow) and W' (shown in red) bands. The overlapping area is about 512×360 pixel and covers $\delta = -61.7^{\circ} \sim -61.0^{\circ}$. Lower: The sky coverage of the AIRBT Early Data Release (red) and the full data set (gray) in 2025. The blue line is the Galactic plane.

plane, including $\sim 20,000$ images and sky coverage of $\sim 20 \text{ deg}^2$, as the red markers shown in the lower panel of Fig. 2.

3. DATA REDUCTION

In the image reduction, we subtracted the background, divided by the twilight flat and the photometric flat (also known as the star flat), and performed aperture photometry and astrometry. To make reference stars for the W' band, we transformed J and H magnitudes to W' magnitudes as a preliminary photometric calibration.

3.1. Preprocessing and aperture photometry

As shown in the left panel of Fig. 3, the background of the raw images exhibits significant noise, including bias fixed patterns, dark current, warm pixels, and sky background nonuniformity. The usual procedure to correct such background is to acquire bias and dark frames and subtract them from the raw images. However, since the telescope was located at an unmanned location in the center of Antarctica and lacked a mechanical shutter, we could not obtain dark and bias images.

To determine the background, we took the median of the raw images for each night after 3σ clipping to eliminate stars that naturally cross the field. This background includes bias, dark current, and the sky back-

ground. We subtracted the background image from the raw images taken during that night, and used the Python package SEP (K. Barbary 2016) to further sample and subtract the sky background residuals in the right panel of Fig. 3.

Both the twilight flat and the photometric flat were used in succession to correct spatial response nonuniformity of images. To correct pixel-scale nonuniformity, we used the twilight flat, which was derived from the median of images taken at dawn and dusk. We divided out the large-scale nonuniformity in the twilight flat using SEP to reduce the effects from the twilight gradient and stray light. Then, to correct large-scale nonuniformity, we used a photometric flat (e.g., F. J. Selman 2004), which was computed by tracking the flux variations of stars as they drifted across the image. The photometric flat contained the information of image quality inhomogeneity and possible ice crystals on the lens. Fig. 4 shows the twilight flat, photometric flat, and the FWHM across the FoV.

We used SExtractor (E. Bertin & S. Arnouts 1996) for source extraction and aperture photometry. As shown in the right panels of Fig. 4, the FWHM was close to 2 pixels in the image. In aperture photometry, we adopted a 3 pixels aperture for faint stars and a 6 pixels aperture

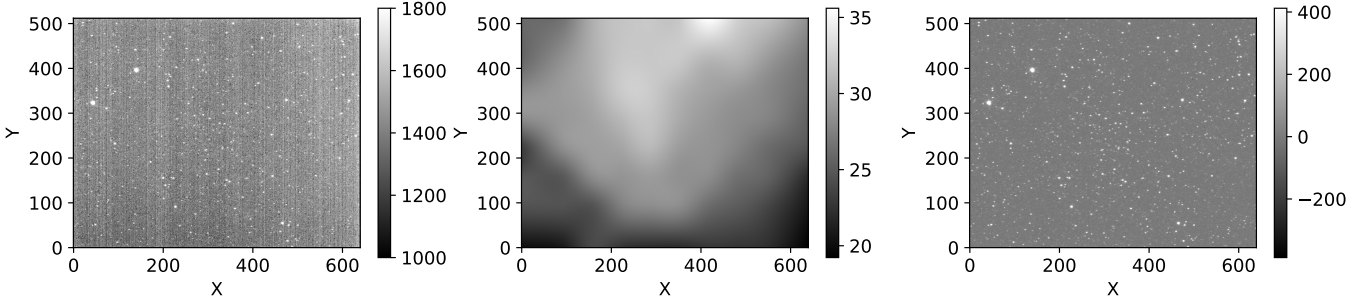


Figure 3. An example of raw (left), sampled sky background residuals from SEP after first background subtraction (middle), and background-subtracted (right) image.

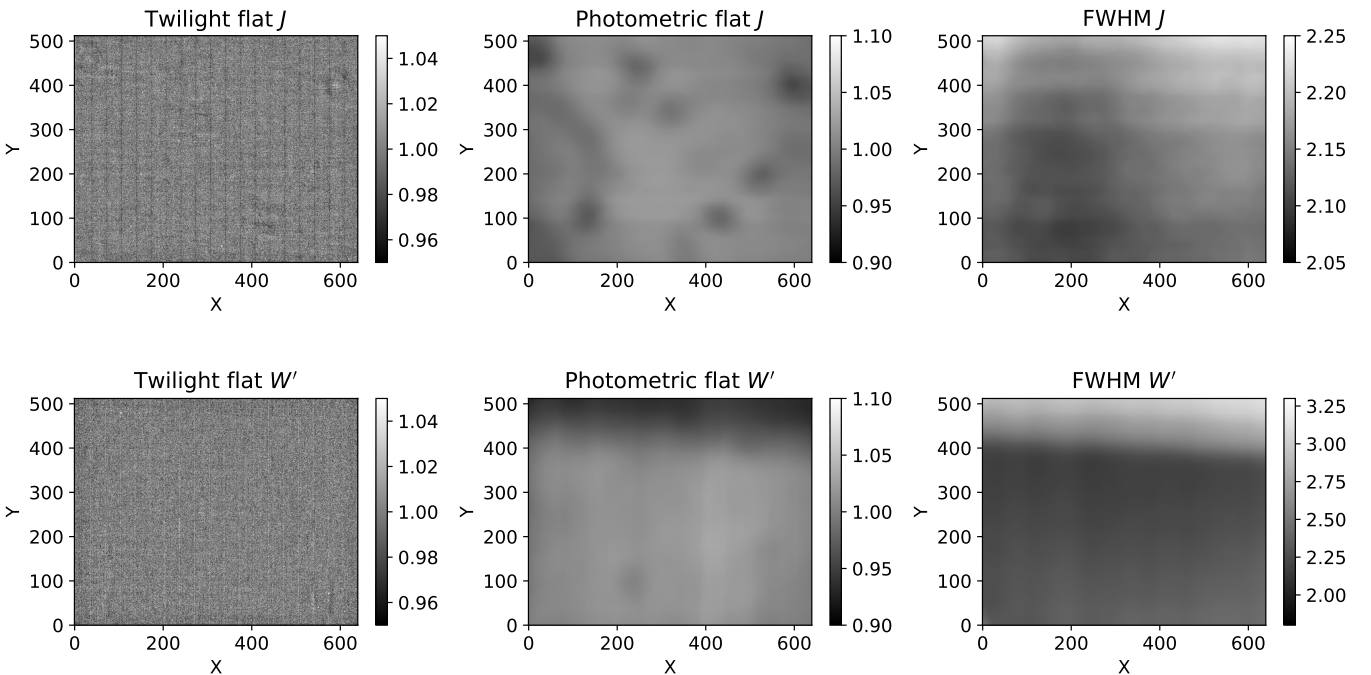


Figure 4. The upper (lower) panels show the twilight flat, photometric flat, and distribution map of the FWHM, respectively, for *J* (*W'*) band. The dark spots in the *J* band photometric flat are likely caused by ice crystals, while the striping in the *W'* band photometric flat is correlated with the striping in the map of FWHM and may be introduced by the *W'* filter, which will be inspected on the next expedition.

for bright stars, to achieve the best signal-to-noise ratio by balancing the star flux and background contamination.

We used SCAMP (E. Bertin 2006) to determine the World Coordinate System (WCS) parameters and took the 2MASS catalog (M. F. Skrutskie et al. 2006) as the astrometric reference. Compared with 2MASS, our astrometric accuracy was $3.8''$.

3.2. Photometric calibration

As a newly designed filter, photometric calibration of *W'* band is essential. The usual procedure is to observe standard stars and use their fluxes for calibration. However, as there are few standard stars within our current

area, in the current processing we derived preliminary *W'* magnitudes by transforming the *J* and *H* magnitudes. A refined calibration either based on standard stars or spectra from SPHEREx (B. P. Crill et al. 2025) will be performed in future work.

In the left panel of Fig. 5, the example spectra of stars earlier than K7 exhibit relatively featureless and straight (on a logarithmic flux scale) near-infrared continua, particularly between the *J* and *H* bands. This makes them suitable for a linear transformation from *J* and *H* magnitudes to *W'* magnitudes. We selected spectra of 186 stars earlier than K7 from the IRTF spectral library (J. T. Rayner et al. 2009; M. C. Cushing et al. 2005; J. T. Rayner et al. 2003) as reference stars. For

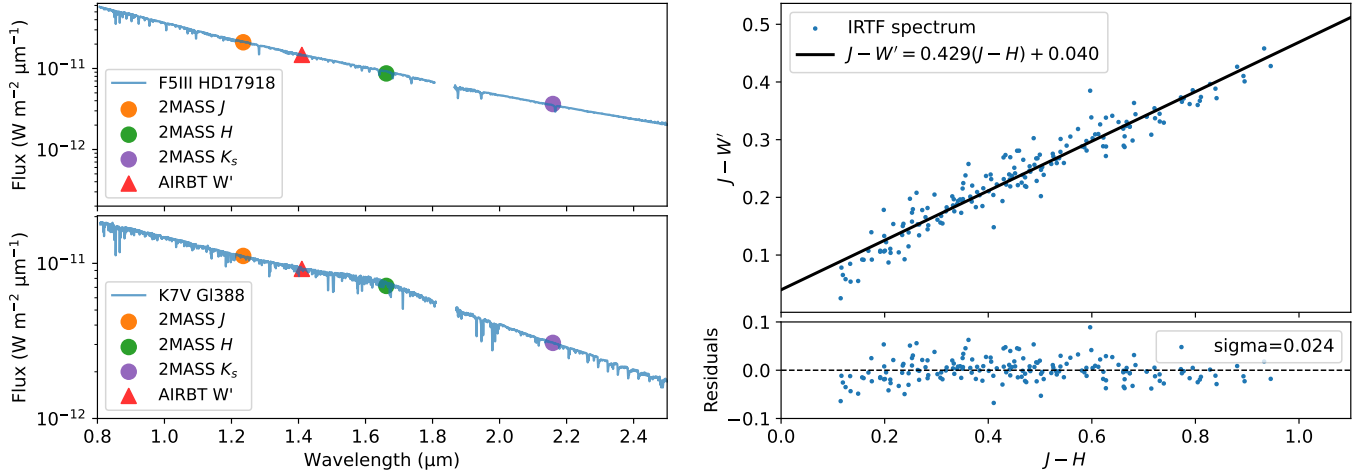


Figure 5. Transformation for W' band. The left upper (lower) panel is the spectrum of F5III HD17918 (K7V Gl388), the orange, green and purple points are fluxes converted from 2MASS J , H and K_s ; the red triangle is the AIRBT W' flux. The right panel is $J - W'$ vs $J - H$ color-color diagram for stars earlier than K7 from the IRTF spectral library, and the black line is a linear fit of it, as the transformation for W' band.

each spectrum, we computed the W' magnitude by convolving the spectrum with the W' filter transmission curve and adopting the Vega flux as the photometric zeropoint. We plot $J - W'$ vs $J - H$ color-color diagram in the right panel of Fig. 5, and derived a linear fitting as the transformation for W' band:

$$W'_{ref} = J - 0.429 \times (J - H) - 0.040. \quad (1)$$

The fitting has an RMS scatter of approximately 0.024 mag, which is sufficient for our preliminary analysis. This transformation is independent of extinction, but only depends on the central wavelengths of the three bands. With the central wavelength of 2MASS J , H and AIRBT W' filters, we derived a slope of $(\lambda_J - \lambda_{W'}) / (\lambda_J - \lambda_H) = 0.42$, which agrees with our fitting in Eq. 1 within the uncertainties.

For calibration of both the J and W' bands, we used the 2MASS catalog as a reference. Since our pixel scale ($6.84''$ pixel $^{-1}$) is much larger than that of 2MASS ($1''$ pixel $^{-1}$), directly cross-matching would introduce significant errors. For AIRBT bright sources with $J = 7 \sim 9$, we find that about 10% (40%) of them are contaminated by more than one additional 2MASS source brighter than 10 (12) mag within their FWHM radius (2 pixels / $13.6''$). Therefore, for each AIRBT source, we searched all 2MASS sources within a radius, summed their fluxes, and then converted it to magnitude as the reference. Since our primary targets are bright stars with a 6 pixels aperture for photometry, we set a matching radius to 3 pixels ($3 \times 6.84''$). As this work represents a preliminary analysis, we adopted this simplified processing strategy. A more detailed calibration procedure will be applied in future analyses of the

full dataset, including down-sampling the 2MASS images and re-performing photometry as a reference catalog.

4. RESULTS

In this section, we present the photometric performance of the J and W' bands images, and describe the EDR. With these data products, we achieve some initial results, including a color-color diagram and variability analysis, which enables a search for candidates with water-vapor-absorption features.

4.1. Data Products

We evaluated our photometric precision by comparing pairs of two consecutive images (each of which is formed from 200 exposures, as previously discussed), which have almost identical conditions and hence the magnitude differences are dominated by photometric errors. For each pair, we cross-matched sources with a separation of less than 1 pixel ($6.84''$) and calculated the magnitude differences. Then in each 0.5 mag bin, we derived the magnitude differences RMS divided by $\sqrt{2}$ as the photometric precision, which is demonstrated in Fig. 6. We also obtained the limiting magnitude at $\sigma = 0.2$. For bright stars, the photometric precision with a 6 pixels aperture reaches 8 mmag in a single frame, which could be further improved by stacking images.

For all 20,000 images in the EDR, we plotted histograms of the FWHM and 5σ limiting magnitudes for J and W' bands in Fig. 7. The median FWHMs are 2.07 and 2.06 pixels for J and W' bands, respectively. The image depth peaks at $J \sim 11.5$ mag and $W' \sim 9.9$ mag. The differences of image quality between the im-

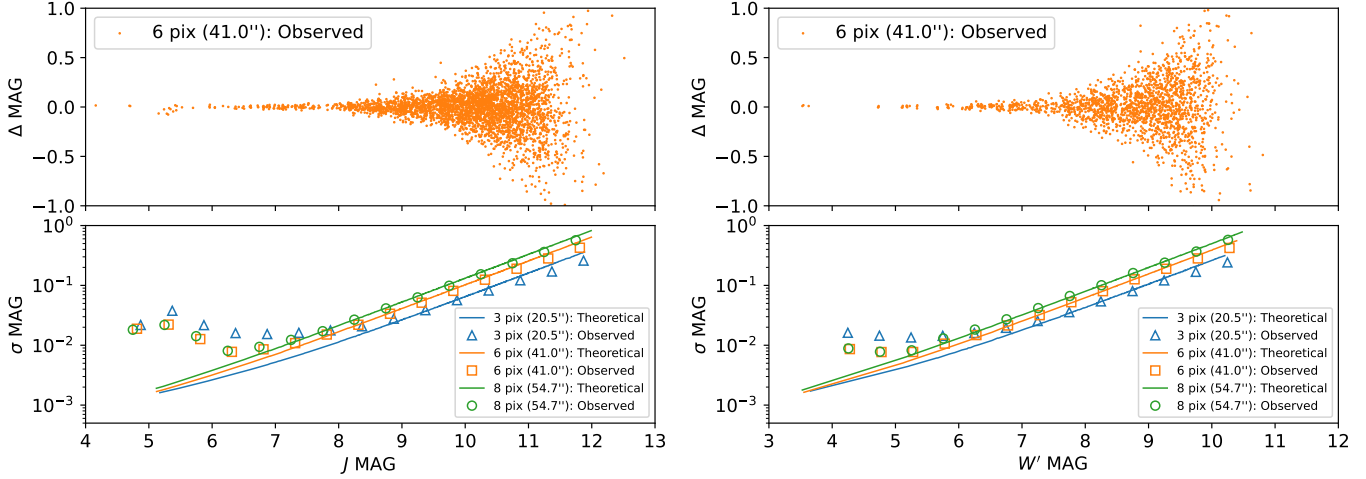


Figure 6. Photometric precision of the J (left) and W' (right) bands. For each band, the upper panel shows ΔMAG vs MAG between pairs of two consecutive images, while the lower panel shows the photometric errors. The observed errors for three aperture sizes were calculated from the RMS of ΔMAG in each 0.5 mag interval divided by $\sqrt{2}$, while the theoretical errors were from SExtractor. In a 2 s exposure, the best photometric precision with a 6 pixels aperture reaches 8 mmag; with a 3 pixels aperture, the limiting magnitudes in the J and W' bands are 11.5 and 9.9, respectively.

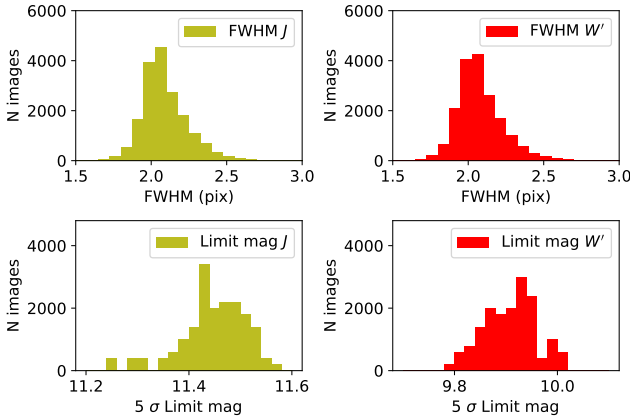


Figure 7. Histograms of the FWHM (upper) and the 5 σ limiting magnitudes (lower) for J (yellow) and W' (red) bands. The peaks of FWHM are close to 2 pix. The peaks of 5 σ limiting magnitudes are 11.5 mag for the J band and 9.9 mag for the W' band.

ages are marginal, demonstrating that both AIRBT and the site conditions at Dome A are stable.

4.2. Color-color Diagram

To characterize water-vapor-absorption features near $1.4 \mu\text{m}$, we plot the $(J - W')_{\text{AIRBT}}$ vs $(J - H)_{\text{2MASS}}$ color-color diagram in Fig. 8. Most sources reside along a line, indicating relatively smooth spectra between the J and H bands. The line has a slope of 0.498, slightly steeper than that in Eq. 1 due to the difference of J between AIRBT and 2MASS as described in Sect. 2. However, a small population deviates downward, implying that their W' magnitudes are larger than expected and

thus they are candidates with water-vapor-absorption features.

To verify this hypothesis, we queried the SIMBAD database for the spectral types of all sources and obtained about 10% with known spectral types (M. Wenger et al. 2000; J. D. MacConnell 1994). We color-coded the sources according to their spectral types in Fig. 8. It is clear that most early type stars (with no absorption features) reside along the line, while most outliers are late M-type stars (probably with absorption features). The color-color diagram is more robust than $J - H$ color alone, which suffers from varying reddening from interstellar extinction.

It is worth emphasizing that the magnitudes from the two bands for each color should be observed simultaneously, otherwise variability of the sources could possibly introduce significant errors as discussed in the next subsection. Therefore, we adopted $J - W'$ from AIRBT and $J - H$ from 2MASS, but did not use $W' - H$ because there was no H in AIRBT in 2025. It is also the reason we did not use the reddening-independent index Q (e.g. K. N. Allers & M. C. Liu 2020), which requires simultaneous J , H , and W magnitudes.

4.3. Variability in J and W' bands

We compared ΔJ and $\Delta W'$ between each pair of the three nights (16 March, 3 April, and 20 April 2025) for all sources, 5% of which had significant variations (> 0.05 mag). Fig. 9 evidently shows that most variable stars exhibit larger variations in W' band and they are distributed around:

$$\Delta W' \sim 1.29 \times \Delta J. \quad (2)$$

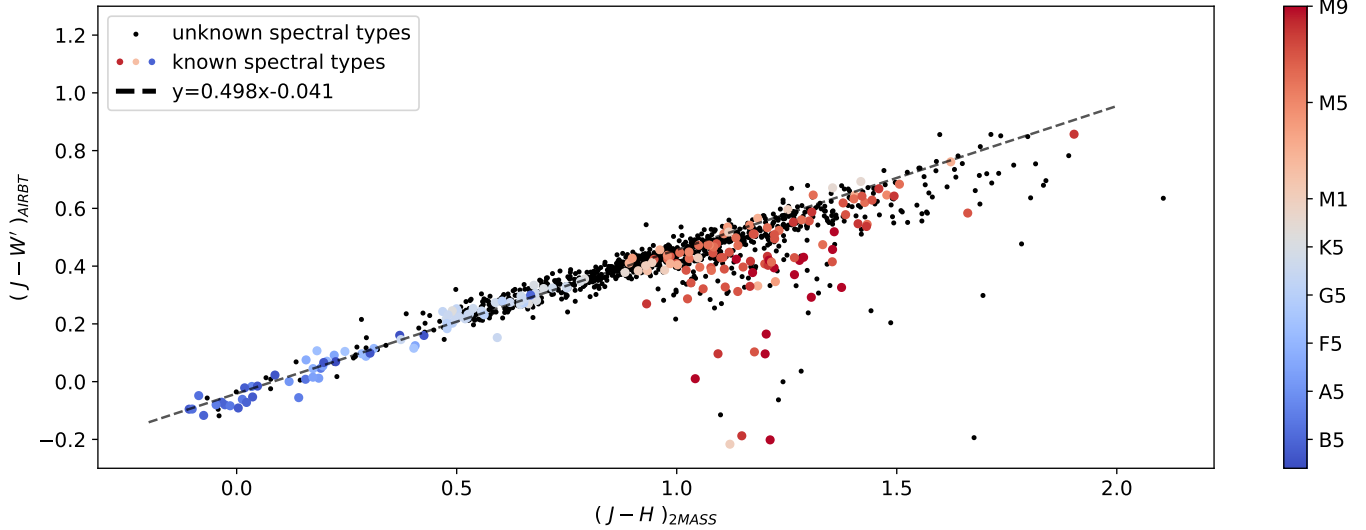


Figure 8. Color-color diagram of $(J - W')_{AIRBT}$ vs $(J - H)_{2MASS}$ from AIRBT data on 3 April 2025. The colored points mark stars with known spectral types from SIMBAD ($\sim 10\%$), and the black points are stars without spectral type information ($\sim 90\%$). The black dashed line is the best fit for AIRBT sources in the range $0 < J - H < 1$.

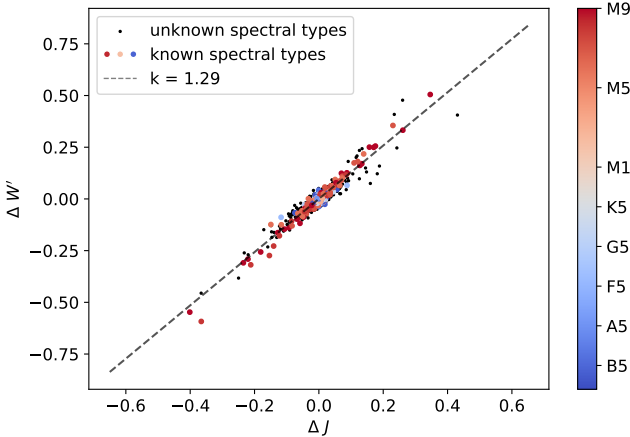


Figure 9. Magnitude variations of J and W' bands between each pair of the three nights of all stars. The colored points mark known stars from SIMBAD ($\sim 10\%$), and the black points are stars without spectral type information ($\sim 90\%$). The black dotted line is the best fit of stars in the range $|\Delta J| > 0.05$ and $|\Delta W'| > 0.05$ ($\sim 5\%$ of the stars).

Furthermore, some known M-type stars tend to show even steeper slopes.

However, variability normally decreases with increasing wavelength, as can be understood from the following argument. For continuum flux, variations are mainly driven by radius and temperature. According to the Stefan-Boltzmann law, radius variations affect J and W' bands equally, satisfying $\Delta J = \Delta W'$. On the other hand, the effect of temperature variation is given by Planck's law, which yields $\Delta W' \sim 0.88\Delta J$ for 1000 K

$< T < 4000$ K. Therefore, when both radius and temperature variations are present, we should have $\Delta W' < \Delta J$.

We propose that the excess $\Delta W'$ comes from variations of water-vapor in the star's atmosphere, thereby causing the absorption rates near $1.4 \mu\text{m}$ to vary. To test this, we used synthetic spectra from the PHOENIX model (T.-O. Husser et al. 2013) to simulate the relationship between ΔJ and $\Delta W'$ produced by temperature variations. Since most of our samples are giants from the Milky Way, we adopted the model parameters for them: $\log g = 1$ and $[M/H] = 0.0$. As shown in Fig. 10, the strength of water-vapor-absorption feature near $1.4 \mu\text{m}$ does vary with temperature. The simulations yield $\Delta W' = (1.4 \sim 2.5)\Delta J$ for M-type giants with $2500 \text{ K} < T < 3200 \text{ K}$, which is consistent with our results. Since our observed variable sources include both early and late type stars, the variation ratio in Eq. 2 lies between the continuum prediction and the PHOENIX model. If the ratio of $\Delta W'/\Delta J$ is larger than 1, it signifies a late-type star.

Discrepancies between ΔJ and $\Delta W'$ may also arise from additional effects. Light curves of ultracool stars would show different phases between J and W' bands because the formation and dissociation of atmospheric water-vapor lag behind the temperature change. Additionally, seasonal variations in W' band could only be present from some ultracool stars under specific conditions. The observed W' flux is a convolution of the stellar spectrum and the telluric atmosphere transmission, both of which contain water-vapor-absorption features. The water-vapor produces many deep (close to 100%) and narrow ($< 1 \text{ nm}$) absorption lines, which are

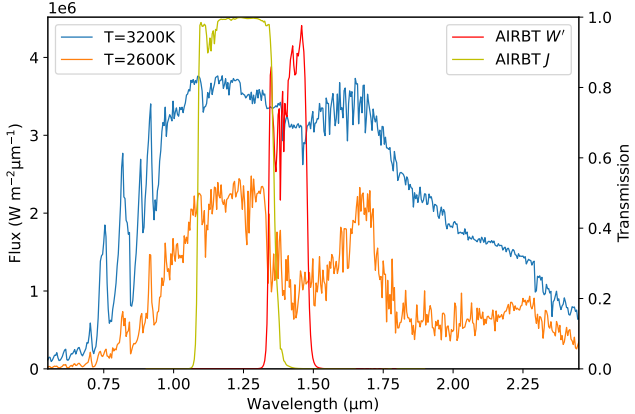


Figure 10. Spectrum variability from the PHOENIX model with $\log g = 1$ and $[M/H] = 0.0$. The blue (orange) line shows spectra of a giant star with temperatures of 3200K (2600K), and the red (yellow) line is the transmission curve of the AIRBT W' (J) filter. The W' filter covers the water-vapor-absorption feature near $1.4 \mu\text{m}$.

already smoothed in Fig. 1. The convolution reaches maximum when both spectra line-up perfectly and drops when they are misaligned. As the apparent radial velocity of the target star varies with Earth’s orbital motion, the W' flux fluctuates accordingly. We will further investigate these effects with well-sampled light curves in the future work.

5. DISCUSSION

In this section, we discuss the scientific applications and potential of the W' band filter. A more detailed analysis will be presented in a future work.

5.1. Optical depth in the $1.4 \mu\text{m}$ band

The strength of water-vapor-absorption can be quantified either by the optical depth τ or by the reddening-independent index Q (e.g. K. N. Allers & M. C. Liu 2020). Here we adopt the optical depth τ and define it as:

$$\tau = \ln \frac{F_{W', \text{cont}}}{F_{W'}} = 0.4 \ln 10 \cdot (W' - W'_{\text{cont}}), \quad (3)$$

where $F_{W'}$ and $F_{W', \text{cont}}$ are the observed W' flux and the continuum W' flux, as shown in Fig. 11.

The W'_{cont} is transformed from J and H magnitudes via Eq. 1. Since AIRBT lacks its own H band observations, we used the 2MASS J and H magnitudes to conduct the transformation. However, as the 2MASS and AIRBT observations are separated by a long period of time, we need to correct the variation of W'_{cont} , which could be as large as 0.5 mag shown in Fig. 9. As established in Sect. 4.3, $\Delta W'_{\text{cont}} \leq \Delta J_{\text{cont}}$. Thus, for the

continuum flux without water-vapor-absorption, we assume that $\Delta W'_{\text{cont}} \approx \Delta J_{\text{cont}}$, and correct the variation for W'_{cont} using

$$W'_{\text{cont}} = W'_{\text{ref}} - \Delta W'_{\text{cont}} \approx W'_{\text{ref}} - (J_{\text{AIRBT}} - J_{\text{2MASS}}), \quad (4)$$

where W'_{ref} is the reference W' magnitude transformed from 2MASS J and H (Eq. 1). For bright stars ($6.5 < J < 9$ and $5.5 < W' < 8$), the uncertainty of τ is ~ 0.05 calculated using error propagation from magnitude errors.

Depressions of the spectrum of ultracool stars near $1.4 \mu\text{m}$ caused by water-vapor-absorption should be detectable as high optical depth. In the left panel of Fig. 12, we plot the optical depth τ against the spectral type for the known M-type stars we observed. For comparison, we also plot τ calculated from spectra from the IRTF spectral library in the right panel. Our observational data show a trend similar to that of IRTF giants: the optical depth τ is ≈ 0 for spectral type M0-M5 and increases for later spectral types (M6 and later).

However, there is a large dispersion in the left and middle panels of Fig. 12, which may be explained by the variation of spectral types, since most of the sources are Mira variables. When a Mira’s brightness decreases, its temperature decreases, the spectral type becomes later, and the water-vapor in the atmosphere increases (D. Boyd 2021; B. J. Smith et al. 2002; M. Matsuhara et al. 2002), and vice versa. Consequently, their spectral types at the epoch of our observation may differ from those when they were classified as late-type stars by D. MacConnell (2010).

We examined 2 examples whose optical depth and spectral type (when they were verified) are inconsistent, as square markers show in the left panel of Fig. 12: one was identified as M8 but had a low optical depth, and the other was identified as M3 but had a high optical depth. We retrieved their optical light curves from Gaia DR3 (Gaia Collaboration et al. 2016). Given that the Gaia DR3 light curve spanned 2015–2017 while our observations were conducted in 2025, we used the Generalized Lomb-Scargle (GLS) method to compute periods and inferred phases at the epoch of AIRBT observations in the right panel of Fig. 12. We find that the inconsistent τ can be explained by the variability: the M8 one was observed by AIRBT at almost peak brightness, indicating a higher temperature, lower water-vapor-absorption and smaller τ . The M3 one was observed close to the minimum brightness, which also leads to the observed differences in τ .

Thus we can use the optical depth τ to estimate stellar spectral types, similarly to the method used by K. N. Allers & M. C. Liu (2020) to estimate spectral types of

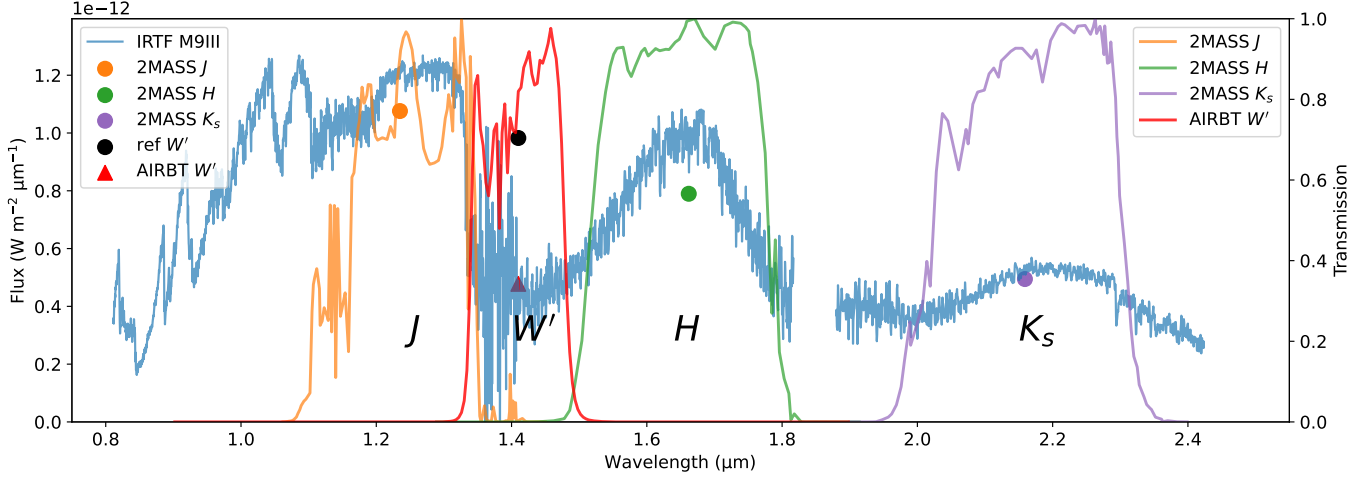


Figure 11. An example showing the calculation of optical depth τ . The blue line is a spectrum of an M9 giant BRIB1219-1336 from the IRTF spectral library, showing a water-vapor-absorption feature near $1.4\ \mu\text{m}$. The orange, green and purple points are the J , H and K_s fluxes converted from 2MASS magnitudes. The black point denotes the reference or continuum W' flux from transformation, and the red triangle is the W' flux obtained by convolving the spectrum with the filter transmission curve. The discrepancy between the expected W' flux and the reference W' flux reflects the water-vapor-absorption feature.

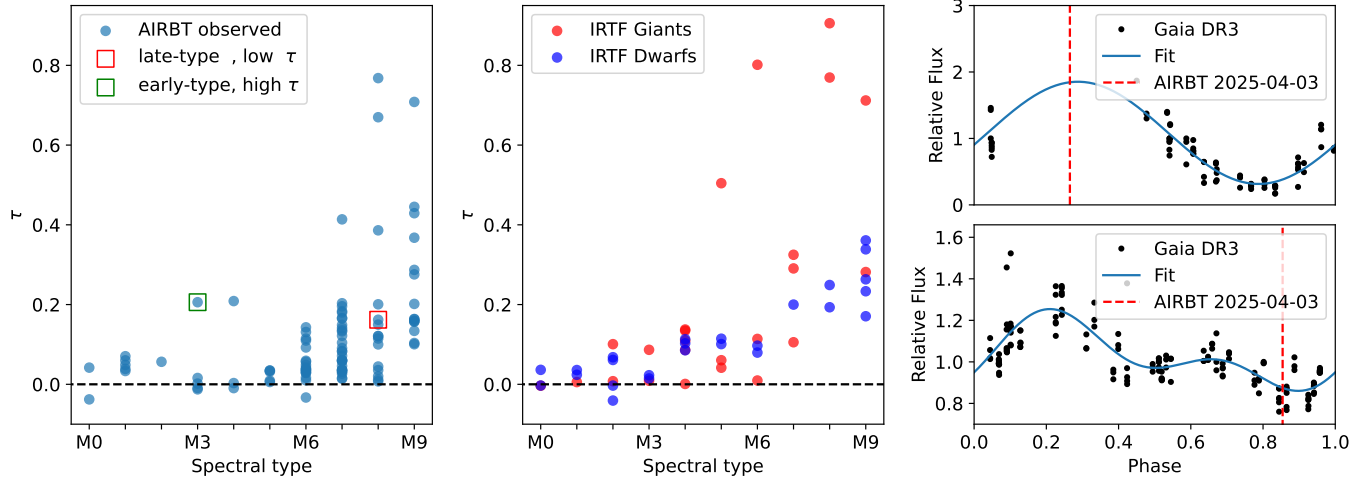


Figure 12. Left: Relationship between optical depth τ and spectral type from AIRBT known M-type stars. Square points mark 2 examples examined in right panel. Middle: Results from IRTF spectral library separated into giants (red) and dwarfs (blue). Right Upper (Lower) panel: Light curve of the M8 giant Gaia DR3 5255960181168967808 (M3 giant Gaia DR3 5335159343746430336), which was identified as late (early) spectral type but shows a low (high) optical depth, and AIRBT observed it at the brighter (fainter) phase indicated by the red dashed line.

late-type dwarfs. However, the fine relationship between τ and spectral type is affected by several factors, such as luminosity class (supergiants, giants, dwarfs) and stellar parameters. We will further explore this relationship using an expanded dataset in a future work.

5.2. Dome A Atmosphere Transmission Stability

The atmosphere transmission would vary as a result of the fluctuation of PWV. For PWV values of 0.05 mm (10%) and 0.268 (90%) at Dome A by C.-L. Kuo (2017), the average transmission of W' band is 89.6% and 75.5%,

respectively (H. Zhang & B. Ma 2024). They correspond to a magnitude difference of 0.08 mag compared to the median PWV.

To verify the atmosphere transmission stability of Dome A, we compared the instrumental magnitudes of stars between 16 March, 3 April, and 20 April 2025. We selected stars with $SNR > 50$ on each of the three nights, cross-matched them, and subtracted instrumental magnitudes to obtain differential magnitudes; the resulting histogram is shown in Fig. 13. The median instrumental magnitude difference with a 6 pixels aperture

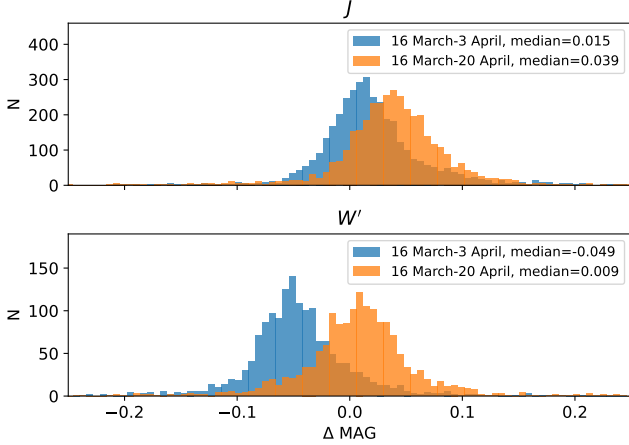


Figure 13. Atmosphere transmission stability for J (upper) and W' (lower) bands at Dome A, Antarctica. The blue (orange) histograms are instrumental magnitude differences with a 6 pixels aperture between 16 March and 3 April (20 April) 2025.

was < 0.05 mag for both J and W' bands, possibly owing to the variations of atmosphere transmission as well as accumulation of marginal frost on the windows. This value agrees well with theoretical predictions above. It demonstrates that the atmosphere transmission for W' band at Dome A is not only high but also stable.

6. CONCLUSION

To take advantage of high atmospheric transmission at Dome A, we designed a new W' filter covers the entire water-vapor-absorption region around $1.4 \mu\text{m}$ and installed it in AIRBT at Dome A in 2025. We selected simultaneous J and W' images from three nights between March and April 2025 as an Early Data Release (EDR) to test the performance of W' band filter. We derived a preliminary calibration for the W' band by transforming J and H magnitudes. And we achieved 5σ limiting magnitudes of $J \sim 11.5$ and $W' \sim 9.9$ for 2 s exposures.

With W' band, we successfully detected candidates with a water-vapor-absorption feature near $1.4 \mu\text{m}$ by two methods. In the $J - W'$ vs $J - H$ color-color diagram, we identified outliers that exhibit lower W' fluxes than expected. In the variability analysis, most of the variable sources are more variable in W' than in J , and we attribute the excess $\Delta W'$ to the variations of the water-vapor-absorption feature. Furthermore, we quan-

tified the absorption by optical depth, τ , and found τ increasing with spectral types for M6 and later. This indicates that our observations can be used to search for ultracool stars and estimate their spectral types.

We verified the atmosphere transmission stability for W' band at Dome A is better than 5%. The high stability indicates that Dome A is a promising site for future observations to study water-vapor in the universe.

We will process all J and W' data obtained in 2025 with fine magnitude calibrations. While most of EDR targets are giants in the Milky Way limited by the single frame depth, we plan to co-add multiple exposures to increase our detection depth by about 3 mag, which enables the future detection of fainter ultracool dwarfs.

In the future, we will replace the telescope's equatorial mount to enable stable pointing and tracking. This will allow us to survey a larger area and observe particular targets, including both scientific sources and standard stars. For the next step, we plan to install a 40 cm telescope equipped with a larger format and lower noise camera. We will also carry out time-domain observations in W' band at Dome A to study the formation and evolution of water-vapor in the universe.

ACKNOWLEDGEMENTS

We are grateful to the 39th, 40th and 41st CHINARE teams supported by the Polar Research Institute of China and the Chinese Arctic and Antarctic Administration. B.M. acknowledges the support from the National Key R&D Program of China (grant No. 2022YFC2807303). We also acknowledge the supports by National Astronomical Observatories, Chinese Academy of Sciences under grant numbers E355350101 and E4TG350101 and by the National Natural Science Foundation of China under grant numbers 11733007 and 12373092. AIRBT is financially supported by School of Physics and Astronomy, Sun Yat-sen University. B.M. acknowledges the support by National Astronomical Data Center, the Greater Bay Area No. 2024B1212080003.

Software: astropy (Astropy Collaboration et al. 2013, 2018, 2022), SEP (K. Barbary 2016), SExtractor (E. Bertin & S. Arnouts 1996), SCAMP (E. Bertin 2006), TOPCAT (M. B. Taylor 2005)

APPENDIX

CATALOG

The final EDR covers $\alpha = 145 \sim 205^\circ$ and $\delta = -61.7 \sim -61.0^\circ$ in both J and W' bands. It consists of three catalogs, one for each night on 16 March, 3 April, and 20 April 2025. Each catalog combines photometric results from ~ 6800 images in J and W' bands. For every source within a night, we take the median photometric results and record the total number of detections in individual frames. Each night includes ~ 15000 identical sources that have more than 30 measurements, corresponding to effective exposure times longer than one minute, to ensure data validity.

The detailed parameters of the catalog are listed in Table 1. The catalog can be accessed via <https://nad.china-vo.org/res/r101738/>.

Table 1. Content of the objects in catalog

Column Name	Type	Unit	Description
RAJ2000	float64	deg	median RA (J2000) of all the source detections in this night
DEJ2000	float64	deg	median Dec (J2000) of all the source detections in this night
Jmag_APER	float32[3]	mag	array of J band photometry MAG_APER at aperture 3,6,8 pixel
e_Jmag_APER	float32[3]	mag	array of the uncertainty of J band photometry MAG_APER at aperture 3,6,8 pixel
FWHM_J	float32	pixel	J band median fwhm of all the source detections in this night
MJD_J	float64	-	J band median MJD (UTC) of all the source detections in this night
AWIN_J	float32	pixel	J band median long axis of all the source detections in this night
BWIN_J	float32	pixel	J band median short axis of all the source detections in this night
errAWIN_J	float32	pixel	uncertainty of J band median long axis of all the source detections in this night
errBWIN_J	float32	pixel	uncertainty of J band median short axis of all the source detections in this night
N_J	int16	-	detections of this source in this night of J band
Wmag_APER	float32[3]	mag	array of W' band photometry MAG_APER at aperture 3,6,8 pixel
e_Wmag_APER	float32[3]	mag	array of the uncertainty of W' band photometry MAG_APER at aperture 3,6,8 pixel
FWHM_W	float32	pixel	W' band median fwhm of all the source detections in this night
MJD_W	float64	-	W' band median MJD (UTC) of all the source detections in this night
AWIN_W	float32	pixel	W' band median long axis of all the source detections in this night
BWIN_W	float32	pixel	W' band median short axis of all the source detections in this night
errAWIN_W	float32	pixel	uncertainty of W' band median long axis of all the source detections in this night
errBWIN_W	float32	pixel	uncertainty of W' band median short axis of all the source detections in this night
N_W	int16	-	detections of this source in this night of W' band
RAJ2000_2MASS	float32	deg	RA (J2000) of the brightest 2MASS source within 3 pixel
DEJ2000_2MASS	float32	deg	DEC (J2000) of the brightest 2MASS source within 3 pixel
Jmag_2MASS	float32	mag	2MASS J band magnitude compute by summarizing flux within 3 pixel
Hmag_2MASS	float32	mag	2MASS H band magnitude compute by summarizing flux within 3 pixel
Kmag_2MASS	float32	mag	2MASS K band magnitude compute by summarizing flux within 3 pixel
Wmag_REF	float32	mag	reference W' magnitude transformed by 2MASS magnitude
e_Jmag_2MASS	float32	mag	uncertainty of 2MASS J band magnitude compute by summarizing flux within 3 pixel
e_Hmag_2MASS	float32	mag	uncertainty of 2MASS H band magnitude compute by summarizing flux within 3 pixel
e_Kmag_2MASS	float32	mag	uncertainty of 2MASS K band magnitude compute by summarizing flux within 3 pixel
e_Wmag_REF	float32	mag	uncertainty of reference W' magnitude transformed by 2MASS magnitude

REFERENCES

Allers, K. N., & Liu, M. C. 2020, Publications of the Astronomical Society of the Pacific, 132, 104401

Ashley, M. C. B., Allen, G., Bonner, C. S., et al. 2010, in EAS Publications Series, Vol. 40, EAS Publications Series, ed. L. Spinoglio & N. Epchtein, 79–84, doi: [10.1051/eas/1040009](https://doi.org/10.1051/eas/1040009)

Astropy Collaboration, Robitaille, T. P., Tollerud, E. J., et al. 2013, *A&A*, 558, A33, doi: [10.1051/0004-6361/201322068](https://doi.org/10.1051/0004-6361/201322068)

Astropy Collaboration, Price-Whelan, A. M., Sipőcz, B. M., et al. 2018, *AJ*, 156, 123, doi: [10.3847/1538-3881/aabc4f](https://doi.org/10.3847/1538-3881/aabc4f)

Astropy Collaboration, Price-Whelan, A. M., Lim, P. L., et al. 2022, *ApJ*, 935, 167, doi: [10.3847/1538-4357/ac7c74](https://doi.org/10.3847/1538-4357/ac7c74)

Barbary, K. 2016, *Journal of Open Source Software*, 1, 58, doi: [10.21105/joss.00058](https://doi.org/10.21105/joss.00058)

Bergin, E. A., & Langer, W. D. 1997, *ApJ*, 486, 316, doi: [10.1086/304510](https://doi.org/10.1086/304510)

Bergin, E. A., & Tafalla, M. 2007, *ARA&A*, 45, 339, doi: [10.1146/annurev.astro.45.071206.100404](https://doi.org/10.1146/annurev.astro.45.071206.100404)

Bertin, E. 2006, in *Astronomical Society of the Pacific Conference Series*, Vol. 351, *Astronomical Data Analysis Software and Systems XV*, ed. C. Gabriel, C. Arviset, D. Ponz, & S. Enrique, 112

Bertin, E., & Arnouts, S. 1996, *A&AS*, 117, 393, doi: [10.1051/aas:1996164](https://doi.org/10.1051/aas:1996164)

Boyd, D. 2021, arXiv preprint arXiv:2107.10061

Ciesla, F. J., & Cuzzi, J. N. 2006, *Icarus*, 181, 178, doi: [10.1016/j.icarus.2005.11.009](https://doi.org/10.1016/j.icarus.2005.11.009)

Cohen, M., Wheaton, W. A., & Megeath, S. 2003, *The Astronomical Journal*, 126, 1090

Crill, B. P., Bach, Y. P., Bryan, S. A., et al. 2025, arXiv preprint arXiv:2505.24856

Cushing, M. C., Rayner, J. T., & Vacca, W. D. 2005, *ApJ*, 623, 1115, doi: [10.1086/428040](https://doi.org/10.1086/428040)

Dong, Z., Ma, B., Zhang, H., et al. 2025, *Publications of the Astronomical Society of the Pacific*, 137, 125003

Dressel, L., et al. 2016, Baltimore: STScI

Fraine, J., Deming, D., Benneke, B., et al. 2014, *Nature*, 513, 526

Gaia Collaboration, Prusti, T., de Bruijne, J. H. J., et al. 2016, *A&A*, 595, A1, doi: [10.1051/0004-6361/201629272](https://doi.org/10.1051/0004-6361/201629272)

Hu, Y., Hu, K., Shang, Z., et al. 2018, *Publications of the Astronomical Society of the Pacific*, 131, 015001

Husser, T.-O., Wende-von Berg, S., Dreizler, S., et al. 2013, *Astronomy & Astrophysics*, 553, A6

Krijt, S., Kama, M., McClure, M., et al. 2023, in *Astronomical Society of the Pacific Conference Series*, Vol. 534, *Protostars and Planets VII*, ed. S. Inutsuka, Y. Aikawa, T. Muto, K. Tomida, & M. Tamura, 1031, doi: [10.48550/arXiv.2203.10056](https://doi.org/10.48550/arXiv.2203.10056)

Kuo, C.-L. 2017, *The Astrophysical Journal*, 848, 64

Lawrence, J., Ashley, M., Hengst, S., et al. 2009, *Review of Scientific Instruments*, 80

Ma, B., Shang, Z., Hu, Y., et al. 2020, *Nature*, 583, 771

MacConnell, D. 2010, *VizieR Online Data Catalog*, 3170, III

MacConnell, J. D. 1994,, *VizieR On-line Data Catalog: III/170A*. Originally published in: (unpublished, 1993; revised 2009)

Matsuura, M., Yamamura, I., Cami, J., Onaka, T., & Murakami, H. 2002, *Astronomy & Astrophysics*, 383, 972

McCullough, P., Crouzet, N., Deming, D., & Madhusudhan, N. 2014, *The Astrophysical Journal*, 791, 55

Radica, M., Welbanks, L., Espinoza, N., et al. 2023, *Monthly Notices of the Royal Astronomical Society*, 524, 835, doi: [10.1093/mnras/stad1762](https://doi.org/10.1093/mnras/stad1762)

Rayner, J. T., Cushing, M. C., & Vacca, W. D. 2009, *ApJS*, 185, 289, doi: [10.1088/0067-0049/185/2/289](https://doi.org/10.1088/0067-0049/185/2/289)

Rayner, J. T., Toomey, D. W., Onaka, P. M., et al. 2003, *PASP*, 115, 362, doi: [10.1086/367745](https://doi.org/10.1086/367745)

Ros, K., & Johansen, A. 2013, *A&A*, 552, A137, doi: [10.1051/0004-6361/201220536](https://doi.org/10.1051/0004-6361/201220536)

Selman, F. J. 2004, in *Optimizing Scientific Return for Astronomy through Information Technologies*, Vol. 5493, SPIE, 453–459

Shang, Z. 2020, *Research in Astronomy and Astrophysics*, 20, 168

Shi, S.-C., Paine, S., Yao, Q.-J., et al. 2016, *Nature Astronomy*, 1, 0001

Sims, G., Ashley, M. C. B., Cui, X., et al. 2012, *Publications of the Astronomical Society of the Pacific*, 124, 74, doi: [10.1086/664077](https://doi.org/10.1086/664077)

Skrutskie, M. F., Cutri, R., Stiening, R., et al. 2006, *The Astronomical Journal*, 131, 1163

Smith, B. J., Leisawitz, D., Castelaz, M. W., & Luttermoser, D. 2002, *The Astronomical Journal*, 123, 948

Taylor, J., Radica, M., Welbanks, L., et al. 2023, *Monthly Notices of the Royal Astronomical Society*, 524, 817, doi: [10.1093/mnras/stad1547](https://doi.org/10.1093/mnras/stad1547)

Taylor, M. B. 2005, in *Astronomical Society of the Pacific Conference Series*, Vol. 347, *Astronomical Data Analysis Software and Systems XIV*, ed. P. Shopbell, M. Britton, & R. Ebert, 29

van Dishoeck, E. F., Bergin, E. A., Lis, D. C., & Lunine, J. I. 2014, in *Protostars and Planets VI*, ed. H. Beuther, R. S. Klessen, C. P. Dullemond, & T. Henning, 835–858, doi: [10.2458/azu_uapress_9780816531240-ch036](https://doi.org/10.2458/azu_uapress_9780816531240-ch036)

van Dishoeck, E. F., Herbst, E., & Neufeld, D. A. 2013, *Chemical Reviews*, 113, 9043, doi: [10.1021/cr4003177](https://doi.org/10.1021/cr4003177)

van Dishoeck, E. F., Kristensen, L. E., Mottram, J. C., et al. 2021, *Astronomy & Astrophysics*, 648, A24

Wenger, M., Ochsenbein, F., Egret, D., et al. 2000, *A&AS*, 143, 9, doi: [10.1051/aas:2000332](https://doi.org/10.1051/aas:2000332)

Wittkowski, M., Chiavassa, A., Freytag, B., et al. 2016, *Astronomy & Astrophysics*, 587, A12

Yang, H., Kulesa, C. A., Walker, C. K., et al. 2010,
Publications of the Astronomical Society of the Pacific,
122, 490

Yang, X., Shang, Z., Hu, K., et al. 2021, Monthly Notices of
the Royal Astronomical Society, 501, 3614
Zhang, H., & Ma, B. 2024, in *Ground-based and Airborne*
Instrumentation for Astronomy X, Vol. 13096, SPIE,
2586–2594